



Synthesis and Characterization of Ta-Doped WO₃ Nanomaterials for Their Application as an Efficient Photocatalyst

Iqra Maryam¹ · Tahir Iqbal¹ · Sumera Afsheen² · Atif Mossad Ali³

Received: 8 May 2023 / Accepted: 19 June 2023 / Published online: 29 June 2023

© The Author(s), under exclusive licence to Springer Science+Business Media, LLC, part of Springer Nature 2023

Abstract

For the degradation of MB dye, pure and Ta-doped (1 to 5%) WO₃ nanoparticles (NPs) have been synthesized in the current work. Facile and efficient hydrothermal method has been carried out to synthesize pure and Ta-doped WO₃ NPs. By using SEM, XRD, UV–Vis, PL, FTIR and Raman spectroscopy analysis, the morphological, structural, optical, and spectral features have been addressed. Due to the well-matched ionic radius of Ta⁺⁵ with WO₃, it plays a crucial part in lowering the rate at which photogenerated electron/hole pairs recombine, resulting in band gap reductions of up to 2.12 and 1.9 eV for direct and indirect transitions, respectively. It is worth mentioning that two distinct WO₃ phases monoclinic and hexagonal have been examined in XRD and Raman analysis for 4 and 5 wt% Ta concentrations. The photocatalytic activity of fabricated NPs was examined by irradiation of visible light on MB dye. Due to the smaller size of NPs, the surface-to-volume ratio would be high which introduces more active adsorption sites thus enhancing the photocatalytic activity of the catalyst. Quite interestingly, 3% Ta-doped WO₃ catalyst exhibits optimal results owing to maximal degradation of 91% in 120 min ascribed to the Burstein-Moss Effect. Recyclability and trapping experiments have been performed to check the stability of the optimized catalyst. The remarkable photocatalytic activity of a 3% Ta-doped catalyst demonstrates its potential uses in the treatment of wastewater.

Iqra Maryam and Tahir Iqbal have contributed equally to this work.

✉ Tahir Iqbal
tahir.awan@uog.edu.pk

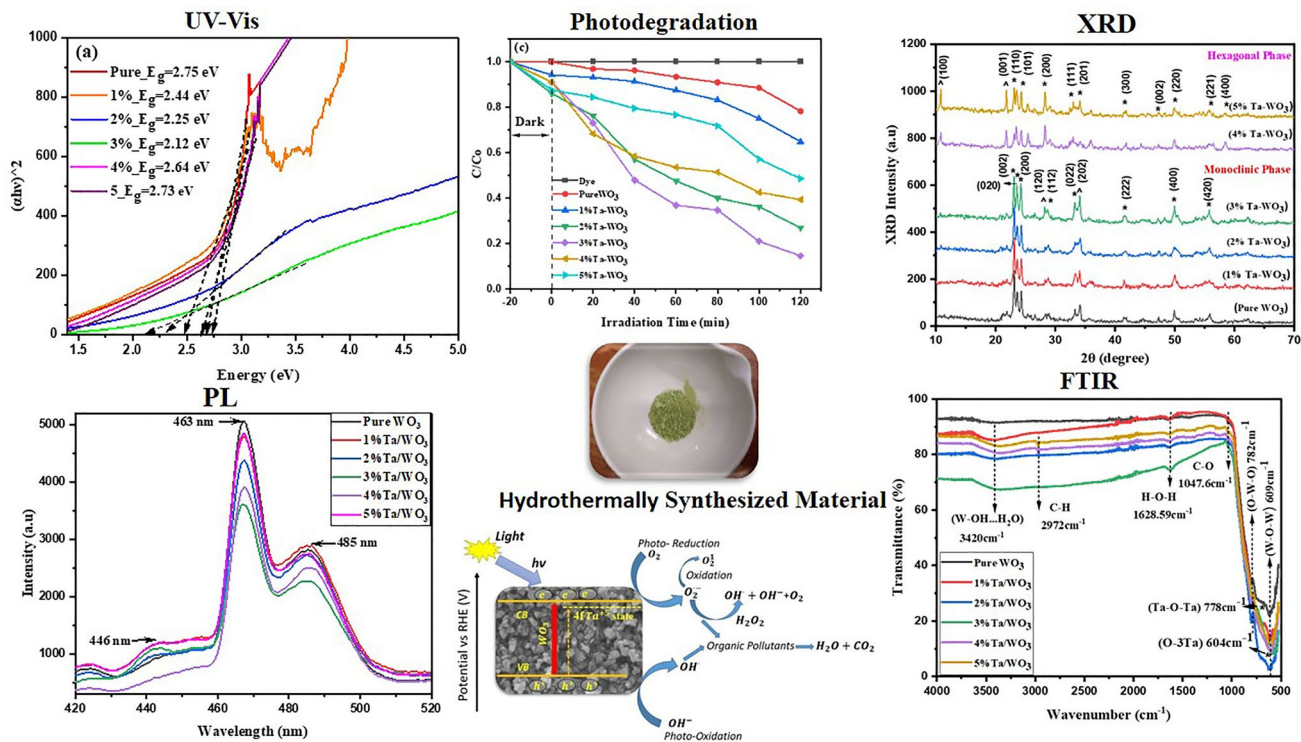
Iqra Maryam
maryamiqra82@gmail.com

¹ Department of Physics, Faculty of Science, University of Gujrat, Hafiz Hayat Campus, Gujrat 50700, Pakistan

² Department of Zoology, Faculty of Science, University of Gujrat, Hafiz Hayat Campus, Gujrat 50700, Pakistan

³ Department of Physics, Faculty of Science, King Khalid University, Abha, Saudi Arabia

Graphical Abstract



Keywords Hydrothermal · Ta-doped WO_3 · Tantalum · Tungsten trioxide · Photocatalytic activity · Methylene blue (MB) dye · Optical properties

1 Introduction

The continuous expansion of industrialization has headed to the rise in energy consumption, resulting in significant environmental pollution problems that have gained widespread attention. In the field of environmental science, the thorough treatment of industrial wastewater has gained importance. To treat wastewater, several traditional techniques have been utilized, including biological treatment, anaerobic, aerobic, and electrochemical treatments, oxidation, reduction, flocculation, flotation, precipitation, and adsorption [1–6]. However, these methods are not always able to completely decompose organic pollutants. Since photocatalysis is both economical and environmentally friendly, it has drawn a lot of attention. Variations in water phases will have a negative impact on the economy, food supply, poverty alleviation, and human health, according to research from the United Nations (UN). It will risk the achievement of goals for world development. Therefore, it is essential to develop wastewater

treatment technologies that are economical, extremely efficient, and environmentally friendly. Organic pollutants in water come in a variety of forms, including organic dyes, phenolic chemicals, and organohalides. These pollutants are difficult to dissolve in water, toxic and even carcinogenic, and chemically resistant. Over 100,000 commercially available dyes are utilized in various sectors. These colors are very harmful to the environment, easily soluble in water, and non-biodegradable. Hence ensuring sustainable energy and environmental protection are critical for achieving economic growth and industrial development. However, the extensive use of fossil fuels, the main source of energy, is rapidly depleting and adding to the problem of global warming [7, 8].

To address this challenge and meet future energy demands without causing harm to the environment, significant progress is necessary in science and engineering. Hence, photocatalysts can utilize light energy to break down water (H_2O) into hydrogen and oxygen, thus producing carbon dioxide

into organic material, and eliminating organic pollutants from water [7, 9]. Therefore, they hold significant potential in addressing the demanding issues of environmental pollution and the energy crisis. Various photocatalysts, including TiO_2 , CdS , WO_3 , C_3N_4 [10], $\text{g-C}_3\text{N}_4/\text{Ag}_2\text{CO}_3/\text{GO}$ [11], $\text{CdS}/\text{CoMoS}_x$ [12], and $\text{Bi}_2\text{MoO}_6/\text{Bi}_2\text{S}_3$ [13], CeVO_4/rGO and $\text{Nd}_2\text{Sn}_2\text{O}_7$ [14, 15], $\text{SmRETi}_2\text{O}_7$ ($\text{RE} = \text{Dy}, \text{Ho}, \text{and Yb}$) [16], $\gamma\text{-MnS}$ [17], $\text{Pr}_2\text{Ce}_2\text{O}_7$ and $\text{Dy}_2\text{O}_3\text{-SiO}_2$ ceramic nanostructures [18, 19], $\text{Dy}_2\text{Ce}_2\text{O}_7$, Zirconia nanostructures, and Nd_2O_3 [20–22], $\text{CoNiWO}_4\text{-gCN}$ [23] and Z-scheme-based novel $\text{CoNiWO}_4/\text{g-C}_3\text{N}_4$ composite [24] have been industrialized. However, they cannot simultaneously have a broad light absorption range and a significant redox ability. Also, single-component photocatalysts frequently fall short of addressing practical requirements [25]. Titanium dioxide (TiO_2) is the most widely researched photocatalyst for water decontamination purposes. However, its application in the field of photocatalysis is greatly limited due to its wide band gap of approximately 3.30 eV, resulting in a small conversion rate in the visible light range [26–29]. When light is present, a substance called a photocatalyst combines with water to create free radicals, which then react with pollutants to degrade them. Additionally, it converts organic contamination into safe compounds without causing any additional pollution issues. The primary drawback of photocatalysis is its high rate of electron/hole recombination and poor photocatalyst light absorption in the visible region. When the bandgap and the rate of electron/hole recombination are suppressed, doping, composites, and heterojunctions are created. Organic compounds, metal oxides, sulphides, etc. can all be used as photocatalysts.

Tungsten trioxide (WO_3) is a semiconductor of transition metal oxide having band gap ranges from 2.4 to 3.0 eV and higher conductivity of $\sim 12\text{cm}^2\text{V}^{-1}\text{s}^{-1}$. This attribute gives WO_3 strong visible-light adsorption ability, which is unlike other photocatalysts like TiO_2 that can only absorb light in the ultraviolet spectral range due to their intrinsic band gap energies [30–32]. Furthermore, WO_3 is highly resistant to photo-corrosion and has stable chemical characteristics [33, 34]. These properties make WO_3 a promising substitute for TiO_2 , which requires modification to absorb visible light. Furthermore, the strongly negative surface charges of WO_3 surfaces make them perfect for adsorption applications, particularly for cationic dyes like methylene blue (MB) [35, 36]. Previous studies show that the amount of catalytic surface-active sites, which are determined by the surface area, light absorption, and structural characteristics of the catalyst, including phase composition, crystallinity, size distribution, and morphology, are primarily related to the rate of degradation of organic substances [37–39]. Among these characteristics, morphological analysis is of particular interest because

the shape and dimensionality of WO_3 can be effectively customized to enhance its photocatalytic properties in practical applications.

The lattice structure of the tungsten trioxide (WO_3) lattice has a considerable impact on the shape and crystal growth direction, which can result in oxygen vacancies in WO_3 . It is significant to remember that doping can influence the band edge locations of WO_3 and enhance characteristics as a photocatalyst, which will increase its photocatalytic degradation of organic pollutants and photoelectrochemical (PEC) activity. For PEC water splitting applications and photocatalytic activity for the degradation of dyes, several metal ions have been utilized to incorporate in WO_3 until now. Song, Bo, et al., reported carbon nanodots based WO_3 to analyze the photocatalytic degradation efficiency. Two-step hydrothermal methods were utilized in this case. Sodium tungstate dihydrate ($\text{Na}_2\text{WO}_4 \cdot 2\text{H}_2\text{O}$) is used as a precursor for the synthesis of WO_3 . Ethanolamine and ascorbic acid have been utilized for the preparation of carbon Nano-dots. From the results, it has been observed that 78% Rhodamine-B dye was degraded [40]. Also, Ta-doped WO_3 was reported by Kalanur, S. S., et al. for enhanced hydrothermal photoelectrochemical water splitting. Ta doping had a significant impact on the shape and crystal structure of WO_3 . SEM images clearly show the nano-triangle morphology of Ta-doped WO_3 . The results of energy dispersive spectroscopy (EDS) show a slight change in the band gap along with the increase in oxygen vacancies. A new approach to crystallography for photocatalytic activity has been presented in this study, which compares the band structure of WO_3 before and after doping it with 1.88% Ta [41].

As mentioned above the Ta-doped WO_3 nanomaterial was previously reported for PEC application but there is no comparative study for photocatalytic photodegradation. Hence, in the present work, introducing Tantalum (Ta) ions into the WO_3 lattice would be a realistic approach because of its well-matched ionic radius (Ta^{+5}) with that of WO_3 , and has been originated to shift the absorption onset of WO_3 towards the visible region. Therefore, in this study, a straightforward hydrothermal approach has been employed to fabricate pure and Ta-doped WO_3 nanoparticles (NPs) with concentrations ranging from 1 to 5% of Ta. The synthesized materials were thoroughly analyzed by numerous techniques, including Scanning Electron Microscopy (SEM), X-ray diffraction (XRD), UV–visible spectroscopy (UV–Vis), Photoluminescence (PL), Raman Spectroscopy, and Fourier-Transform Infrared spectroscopy (FTIR). Also, the photocatalytic degradation of MB dye was examined by using fabricated NPs as an efficient photocatalyst.

2 Experimental Methodology

2.1 Materials

The basic precursor which is utilized for the composition of WO_3 is Sodium Tungstate Dihydrate ($\text{Na}_2\text{WO}_4 \cdot 2\text{H}_2\text{O}$). This base material is purchased from the chemistry department of the University of Gujrat. Hydrochloric acid (HCl) for controlling pH and Ta dopant used in this study is taken from the nano lab of the physics department at the University of Gujrat. Analytical-grade chemicals and reagents were used throughout. All the water used in this investigation was deionized or distilled for stock solutions. All materials used in this study from the chemistry and physics department are $\geq 99\%$ pure from Sigma Aldrich.

2.2 Synthesis Method of Photocatalyst

WO_3 NPs have been synthesized using a variety of techniques, including hydrothermal, solvothermal, sol–gel, and green synthesis. In this study, a facile hydrothermal method is used among others. This selection was made because the hydrothermal process can synthesize nanoparticles with high crystallinity and morphological structure and can function as a one-step synthetic procedure as compared to other techniques. Pure WO_3 was synthesized employing a single-step hydrothermal chemical process. The precursor sodium tungstate dihydrate ($\text{Na}_2\text{WO}_4 \cdot 2\text{H}_2\text{O}$) was utilized to fabricate WO_3 NPs. Initially, 2 g sodium tungstate dihydrate was added to 80 mL of deionized water and put on the magnetic stirrer. This solution was stirred for 1 h at 1500 rev/min. After 1 h of stirring, some drops of hydrochloric acid (HCl) about 2 mL were added to control the pH of the solution and stirred vigorously for again 1 h to get yellow precipitates of

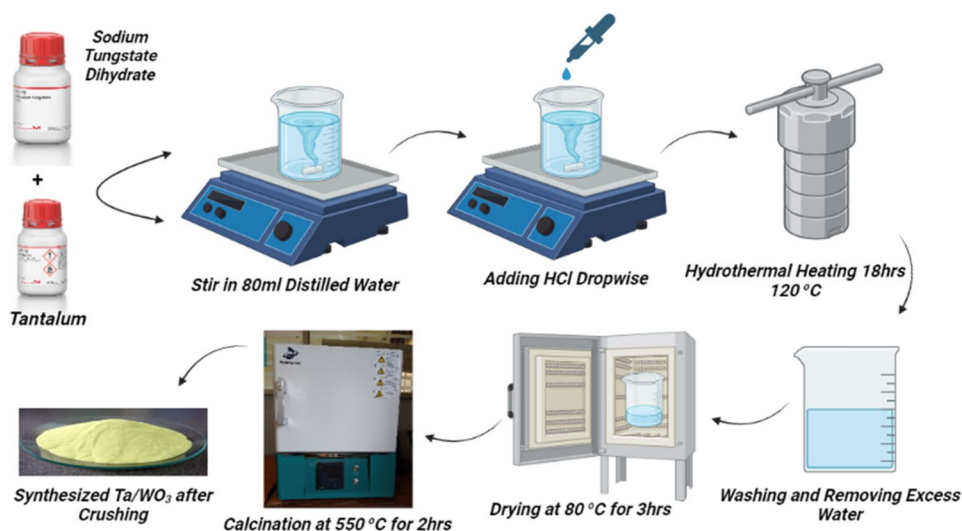
solution. Then synthesized hydrothermal solution of approximately 70% was poured into the Teflon-lined autoclave and transferred into the oven for 18 h at a temperature of 120°C in an electric oven. After 18 h, the resulting solution was washed several times with deionized water and ethanol to balance the pH value. Then, the solution was dried at 80°C for 3 h on the magnetic hot plate. After drying the synthesized material, it was calcinated at 550°C for 2 h. Then after the calcination process, it was kept at room temperature, and then fine crushing of synthesized material was done by mortar and pestle. Finally, pure synthesized WO_3 NPs were obtained.

In the case of Ta-doped WO_3 NPs, 1 to 5% of Ta was doped in WO_3 . For 1% doping, 0.02 g Ta was added in 1.98 g of $\text{Na}_2\text{WO}_4 \cdot 2\text{H}_2\text{O}$ in 80 mL distilled water in the start. The remaining procedure is the same as above for pure WO_3 as shown in Fig. 1. Similarly, for 2%, 3%, 4%, and 5% 0.04, 0.06, 0.08, and 0.10 g Ta dopant in 1.96, 1.94, 1.92, and 1.9 g of $\text{Na}_2\text{WO}_4 \cdot 2\text{H}_2\text{O}$ was utilized respectively.

2.3 Characterizations

To identify the different properties of Ta-doped WO_3 nano-material, different characterization techniques were utilized. For purity and evaluation of the crystallinity of synthesized material was done by utilizing XRD technique. Further, SEM was applied to check the morphology of desired samples. UV–Vis Spectroscopy evaluated the difference in band gap between pure WO_3 and Ta-doped WO_3 . Additionally, PL spectra were observed by using a fluorescence spectrometer. Raman spectroscopy had been used to examine the chemical structure and phases of synthesized NPs. To identify the chemical properties, FTIR was used. Lastly, photocatalytic activity was performed to check the degradation of

Fig. 1 Schematic representation of hydrothermal synthesis for Ta-doped WO_3 nanoparticles



methylene blue (MB) dye by using synthesized pure and Ta-doped tungsten trioxide nanoparticles.

3 Results and Discussion

3.1 Scanning Electron Microscope (SEM)

In SEM analysis, the surface morphology of pure and 3% Ta-doped WO₃ nanoparticles along with the composition of samples were determined. The prepared samples were calcinated at 550 °C. Pure WO₃ reveals the irregularly shaped rough nano-spheroid at different ranges 5, 1, 0.5, and 0.2 μm with different spectral resolutions Fig. 2a, c, e, g while in Ta-doped WO₃ speck of dopant on pure WO₃ was indicated that results in sharp and porous nanocubes of different nanometer range Fig. 2b, d, f, h. Comparison of prepared samples at the same resolution and magnification represents a clear difference in doping material. The morphology, size, and porous nature of nanoparticles of different lengths, sizes, and diameter depends on the synthesized dopant percentage and thermodynamic conditions (temperature, methodology, heat treatment, etc.).

It is worth mentioning that, the histogram plot shows that the size of nanoparticles ranges from 5 to 35 nm and most particles lying in the 17 to 20 nm range in pure WO₃ decrease to the 11 to 15 nm range by adding the concentration of Ta dopant Fig. 2i, j. Additionally, in histogram plots of the area of nanoparticles for pure WO₃ and 3% Ta/WO₃, the average particle size is 17.4 nm which decreases to 12.6 nm respectively which is calculated by ImageJ software Fig. 2 (i, j). Interestingly, the average size of NPs is well correlated with XRD results. These doped agglomerates supported in degradation of organic pollutants from wastewater.

3.2 X-Ray Diffraction (XRD) Evaluations

To determine the dimensions, state, and crystal arrangement of WO₃ as well as its Ta-doped variations for their photocatalytic uses, the tungsten trioxide is infused with tantalum at 1% to 5% concentrations. X-ray diffraction analysis depicts a clear difference between pure WO₃ and Ta-doped WO₃ shown in Fig. 3a. This graph shows two different phases (monoclinic and hexagonal) of Ta-doped WO₃ which depends on the annealing temperature. It is reported that the hydrothermal condensation of the mixture is a well-known method for producing the hydrated orthorhombic WO₃·0.33H₂O stage. This phase remains stable and maintains its chemical and structural properties up to an annealing temperature of 300 °C. However, annealing the material at 400 °C causes chemical dehydration and modification, resulting in the formation of stable bonds thus introducing a hexagonal crystal structure (JCPDS no. 75–2187) Fig. 3a.

When the annealing temperature is raised to 500 °C or above, the hexagonal crystal phase is transformed completely into the stable monoclinic phase (JCPDS no. 43–1035) via a reconstructive transformation [41]. In the present situation, prepared samples are annealed at 550 °C among which 1% to 3% show monoclinic phase but 4% and 5% show hexagonal phase. This is because the reconstructive transition is complicated by an increase in Ta ions in the WO₃ crystal lattice. Prior research on Ti-doped WO₃ revealed these phenomena of multiple-phase development, which produced a blend of hexagonal and monoclinic phases [42]. Hence, in the XRD pattern “*” shows the peaks of WO₃, and “^” shows a slight change peaks due to different doping concentrations but the overall crystallographic structure is the same. On the plane (002), the prepared samples have a preferred orientation $i-e 2\theta=24.418^\circ$ which represents a slight decrease in intensity with the increase in Ta concentration for the monoclinic phase Fig. 3b. It is worth mentioning that crystallographic structure is not affected by dopant concentration of 1 to 3% this is due to the fact of the similar structure of tantalum and tungsten. The average crystallite size (D) of nanoparticles is estimated by the Scherrer formula:

$$D = \frac{k\lambda}{\beta \cos\theta} \quad (1)$$

In above Eq. (3), $\epsilon D \epsilon$ represents crystallite size, $\epsilon k = 0.96 \epsilon$ constant, $\epsilon \lambda = 0.15406 \text{ nm} \epsilon$ indicates the wavelength of source of x-rays, $\epsilon 2\theta \epsilon$ is angle of diffraction and full width half maximum (FWHM) is denoted by $\epsilon \beta \epsilon$ which estimates the peaks of maximum intensity. The average $\epsilon D \epsilon$ of nanoparticles is 15.72 and 11.32 nm for pure and 3% Ta-doped WO₃ that is well correlated with SEM analysis.

3.3 UV–Vis Spectroscopy Evaluations

The UV–Vis spectra of pure WO₃ and Ta-doped WO₃ were measured using the UV–Vis double-beam spectrometer (Double Beam UV–Vis Spectrophotometer SP-IUV&, UOG). These materials are concerned with flaws and optical band gaps that depend on absorbance. According to the Tauc plots, the band gap was 2.75 eV for pure WO₃, 2.44 eV, 2.25 eV, 2.12 eV, 2.64 eV, and 2.73 eV for 1%, 2%, 3%, 4%, and 5% Ta-doped WO₃ respectively for direct transitions Fig. 4a whereas in case of indirect transitions band gaps are slightly different for both pure WO₃ and Ta-doped WO₃. The band gap of pure WO₃ is 2.64 eV and 2.29 eV, 2.1 eV, 1.9 eV, 2.58 eV and 2.6 eV for 1%, 2%, 3%, 4%, and 5% Ta-doped WO₃ respectively Fig. 4b. The band gap was reduced when we added 1, 2, and 3% Ta to WO₃ but at 4% Ta doping, the band gap was again increased, which perfectly illustrates the presence of Ta⁺⁵ ions in the WO₃ lattice. This is due to the Burstein-Moss effect, according

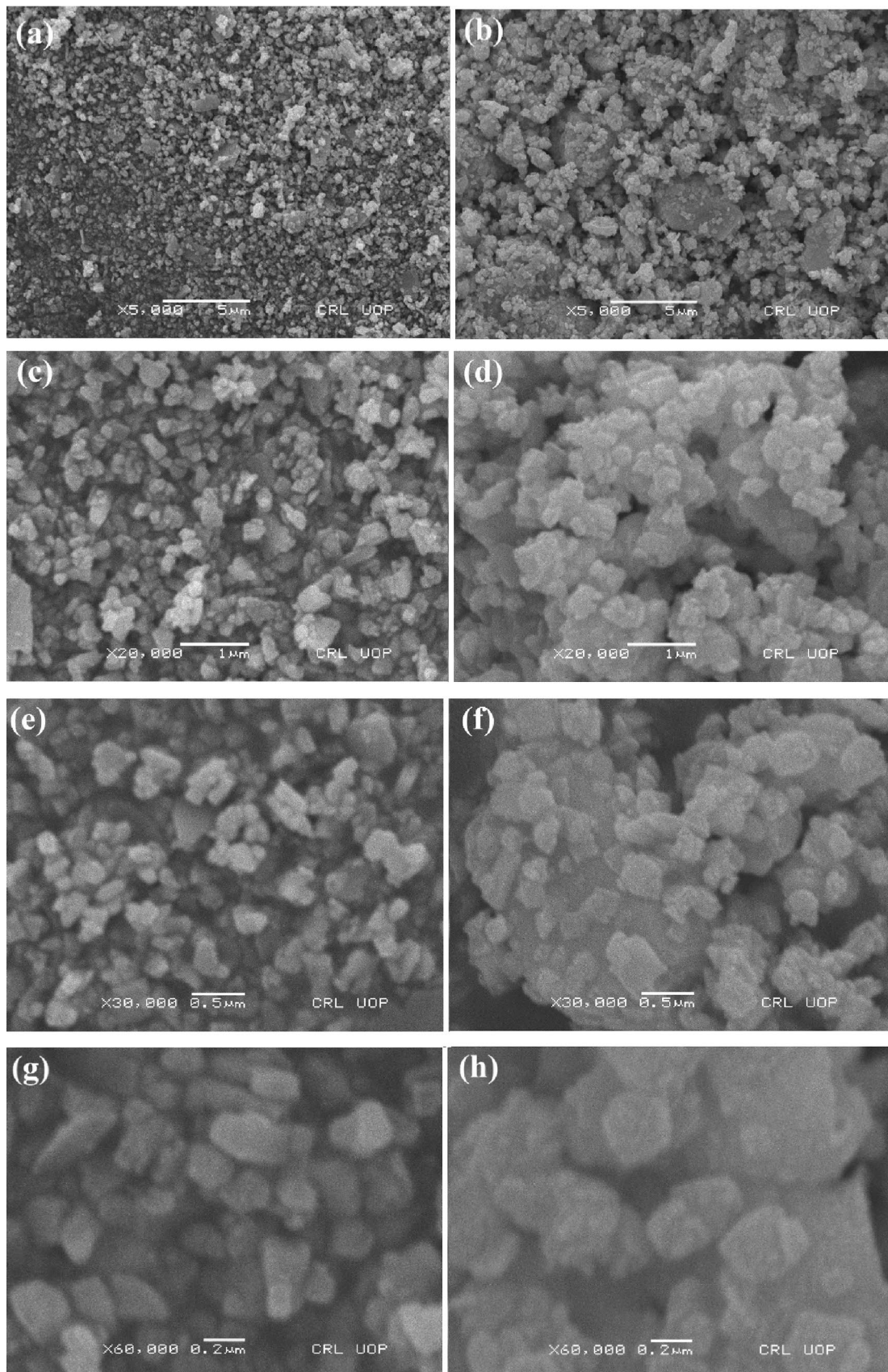


Fig. 2 a, c, e, g SEM images of pure WO_3 . b, d, f, h SEM images of 3% Ta-doped WO_3 nanoparticles. i, j Histograms plots represent average size of NPs for pure and 3% Ta/ WO_3

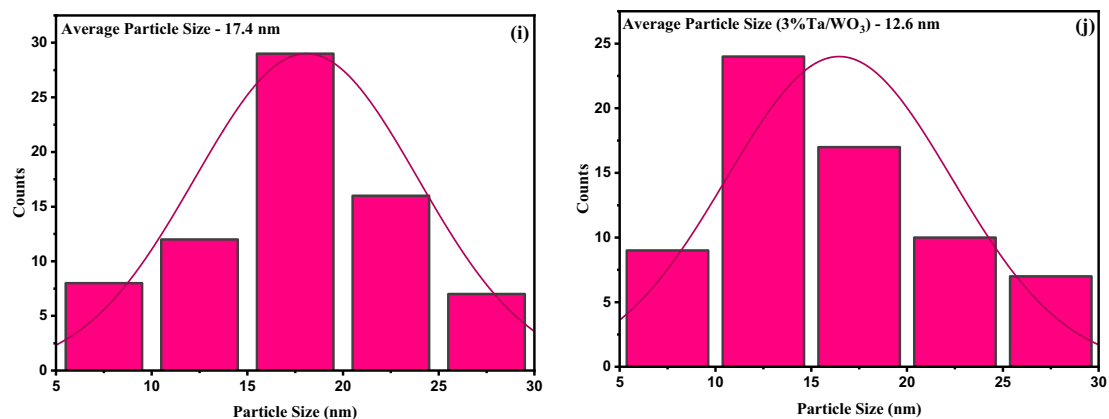
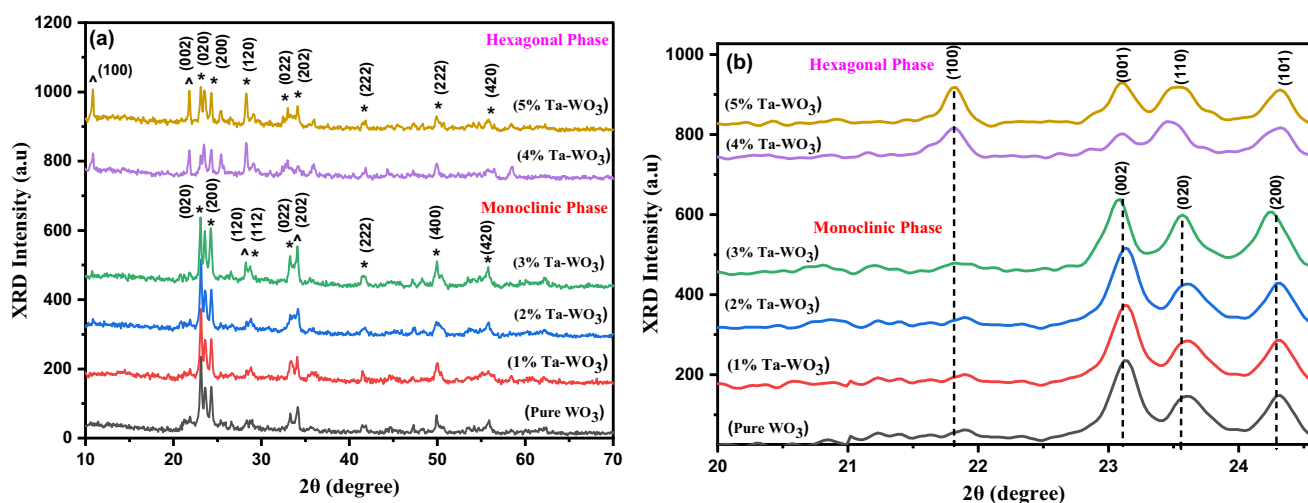
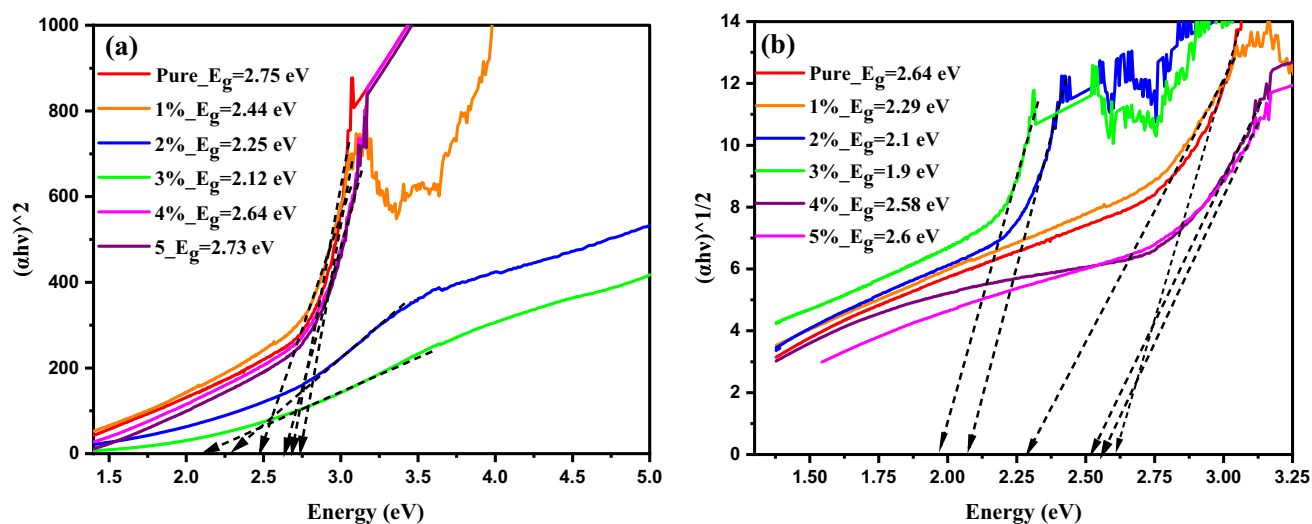


Fig. 2 (continued)

Fig. 3 a, b XRD spectrum of pure WO_3 and Ta-doped WO_3 which represents slight reduction in intensityFig. 4 UV-vis spectroscopy measurements for pure Ta-doped WO_3 . **a** Represents band gap values for direct transitions. **b** Illustrates for indirect transitions

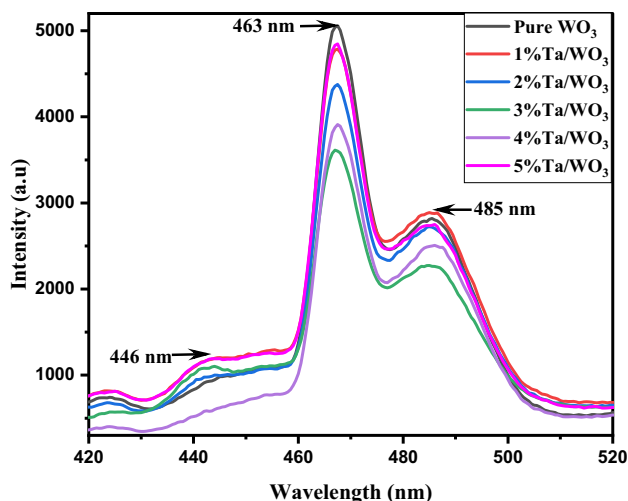


Fig. 5 PL spectra measurements for pure and Ta-doped WO₃

to which the fermi energy level moves towards the valence band and causes a blue shift, increasing the visible band-gap of semiconductor material, at a specific concentration of impurity atoms. Hence, we can say that 3% Ta in WO₃ is considered as efficient comparatively. The nanoparticles of WO₃ also undergo phase shifts as a result. This is caused by an increase in the concentration of doping, which shifts the electron's stimulation and excitation from the valence band (VB) to the conduction band (CB).

Mathematical relation for the calculation of direct and indirect band gap is given as:

For direct band gap,

$$(ah\nu)^2 = K(h\nu - E_g) \quad (2)$$

For indirect band gap,

$$(ah\nu)^{1/2} = K(h\nu - E_g) \quad (3)$$

Here, $h\nu$ is for photon's energy, A is constant, and E_g indicates the band gap of the samples. This modification of the absorbance level and band gap energies validates the value of Ta in improving the optical characteristics of the WO₃ material. Additionally, a smaller band gap can improve the desired samples photocatalysis performance.

3.4 Photoluminescence Evaluations

In photoluminescence (PL) measurements, using photoluminescence spectroscopy (PL: RAMANLOG 6, UOG), the material's imperfections have been identified. The maximal rate of photogenerated $e^- - h^+$ pair recombination in the materials is often indicated by a greater PL intensity [52]. For synthesized Ta-doped WO₃ samples, PL spectra revealed continuous emission with 340 nm excitation

wavelength which is presented in Fig. 5. When compared to doped WO₃, wide emission peaks with a centre at 463 nm can be seen in pure WO₃ with higher intensity, suggesting a quicker rate of $e^- - h^+$ pair recombination. The blue emission at 485 nm is because of the band-to-band transitions in WO₃ and is well matched with literature [43, 44]. However, when doping concentration was added, the intensity of the PL decreased. At 3% Ta-doped WO₃ nanoparticles minimal PL intensity was noticed but at 4% and 5% doping again the band gap starts increasing accordingly. The band gap of 2.75 eV, which is appropriate for WO₃, is given by the first wavelength peak 446 nm which is well correlated with Tauc plot band gap calculations. We may learn about the contaminants in the samples from the second peak.

It is thought that the dopant causes a decrease in the rate of $e^- - h^+$ pair recombination. This is because the dopant generates a new trapping defect site, which may significantly lessen the trapping of electrons in oxygen vacancies, and the h^+ transport in WO₃ will result in significantly reduced photogenerated charge carrier recombination. The photocatalytic activity of 3% Ta-doped WO₃ is improved by the smaller energy gap and low $e^- - h^+$ pair recombination. The results from the UV-Vis spectra and the published literature are nicely aligned with the required PL spectra.

3.5 Raman Spectroscopy

The lattice deformation caused by the defect states (W^{5+}) produced is confirmed by Raman analysis. Figure 6 displays the Raman spectra of Ta-doped and pure WO₃, highlighting the stretching and bending modes of WO₃ in the absence of an additional Ta-O bond. While frequencies between 600 and 900 cm^{-1} are related to O-W-O stretching modes, frequencies 100 to 300 cm^{-1} show O-W-O bending modes and

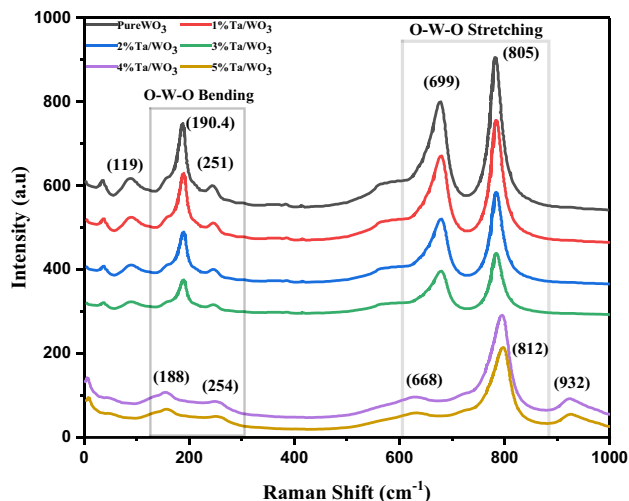


Fig. 6 Raman Spectra analysis for pure and Ta-doped WO₃

the peak at 251 cm^{-1} corresponding to the O-W-O stretching mode of the bridging oxygen ($\text{W}^{+5}\text{-O}$). At normal temperature, a possible combination of monoclinic phases is indicated by the peaks 190.4 , 251 , 699 and 805 cm^{-1} . The synthesized samples for Raman spectra are shown in Fig. 6 and exhibit two distinct peaks at 699 cm^{-1} , and 805 cm^{-1} , both of which are due to the O-W-O stretching modes. The distinctive peaks of WO_3 broaden as the dopant concentration rises, with a slight shift of peaks towards lower wavenumbers, indicating a reduction in WO_3 crystallinity, which is expected as well to increase oxygen vacancies. Moreover, peaks at 932 , 254 , and 188 cm^{-1} for 4 and 5 wt% of Ta represent hexagonal structure [45, 46] which is well correlated with XRD results of two different phases.

3.6 Fourier Transform Infrared Spectroscopy (FTIR)

In FTIR spectra analysis, the pure and Ta-doped WO_3 nanostructures at various concentrations 1%, 2%, 3%, 4%, and 5% respectively were evaluated in the region $500\text{--}4000\text{ cm}^{-1}$. These spectra indicate a broad absorption band that confirms the presence of WO_3 at room temperature. The peaks at 609 cm^{-1} and 782 cm^{-1} ascribed W-O-W and O-W-O stretching vibrations [46, 47]. The spectra reveal the presence of water molecules at the surface of WO_3 by hydrogen holding that shows the bends wavelength 3420 cm^{-1} W-OH... H_2O . Moreover, bends at 1628.59 cm^{-1} and the crests at 1047.66 cm^{-1} identify the H-O-H and C-O stretching modes. Now, it is worth mentioning that since the amount of Ta dopant is small enough, very small peaks at 604 cm^{-1} and 778 cm^{-1} ascribed the O-3Ta and Ta-O-Ta bond stretching vibrations which confirms the presence of Ta doping in pure WO_3 Fig. 7. More interestingly, 4 and 5% doping of Ta turns into a hexagonal phase as indicated in the XRD pattern [48–50].

3.7 Enhanced Photocatalytic Activity

A 400 W power metal halide lamp was utilized in a homemade photocatalytic reactor to consider the efficiency of dye degradation of synthesized samples. Basically, WO_3 was considered to be a highly effective catalyst for photocatalytic activity [51]. The experiment involved adding 0.1 mg of MB dye to 100 ml of distilled water and stirring it in a dark room for 20 min. Next, 0.01 g of pure WO_3 catalyst was put in the dye solution, which was then set down in the reactor. After every 20 min, a 5 ml sample was extracted from the solution and subjected to UV-Vis double beam spectrum analysis. This process was repeated for 120 min. The same procedure was repeated for Ta-doped WO_3 to determine the percentage degradation efficiency of the prepared catalysts, using the following formula:

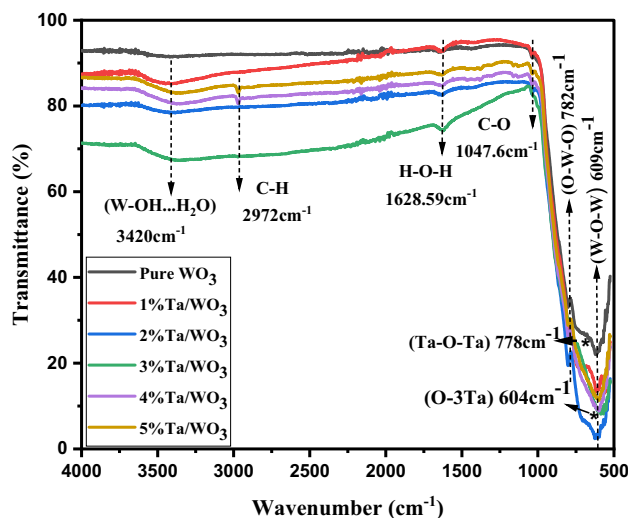


Fig. 7 FTIR spectra of pure and doped WO_3 at different concentrations of tantalum

$$\text{Degradation Efficiency}(\%) = \left(1 - \frac{C}{C_o}\right) \times 100 \quad (4)$$

$$\text{Rate constant}(k) = \ln(C_o/C)/t \quad (5)$$

where C_o is the initial concentration and C is the concentration of dye after time t . Figure 8a displays the UV-Vis spectra of pure and Ta-doped WO_3 in MB dye at 90 min, where the absorption peak shifts downwards as the time interval increases, indicating the degradation of MB. In the degradation process, it is observed in Fig. 8a that among all concentrations of Ta 3% doping in WO_3 is the most efficient one. Hence it is worth mentioning that in 3% Ta-doped WO_3 , the degradation efficiency increased with time and shifted towards the visible range of light, attributable to an optimized decrease in the band gap of the synthesized nanomaterials. In this study, 1%, 2%, 3%, 4%, and 5% Ta-doped WO_3 nanoparticles degraded 35%, 73%, 91%, 60%, and 51% methylene blue (MB) respectively. It is observed that 3% Ta-doped WO_3 degraded most of the MB dye in 120 min comparatively Fig. 8b because degradation efficiency directly relates to the exposure period as shown in Fig. 8c. This is attributed to Burstein-Moss Effect which is described in UV-Vis analysis. Additionally, first-order kinetics are applied on results from which rate constant has been calculated using Eq. (5) and correlation coefficient R^2 (Table 1) has been evaluated by linear fitting using Origin 2021 that represents the strength of linear correlation between different quantities that is optimal for 3% Ta-doped WO_3 nanoparticles Fig. 8d.

Moreover, during photocatalytic activity, the excitation of valence band electrons occurs when the photocatalyst is

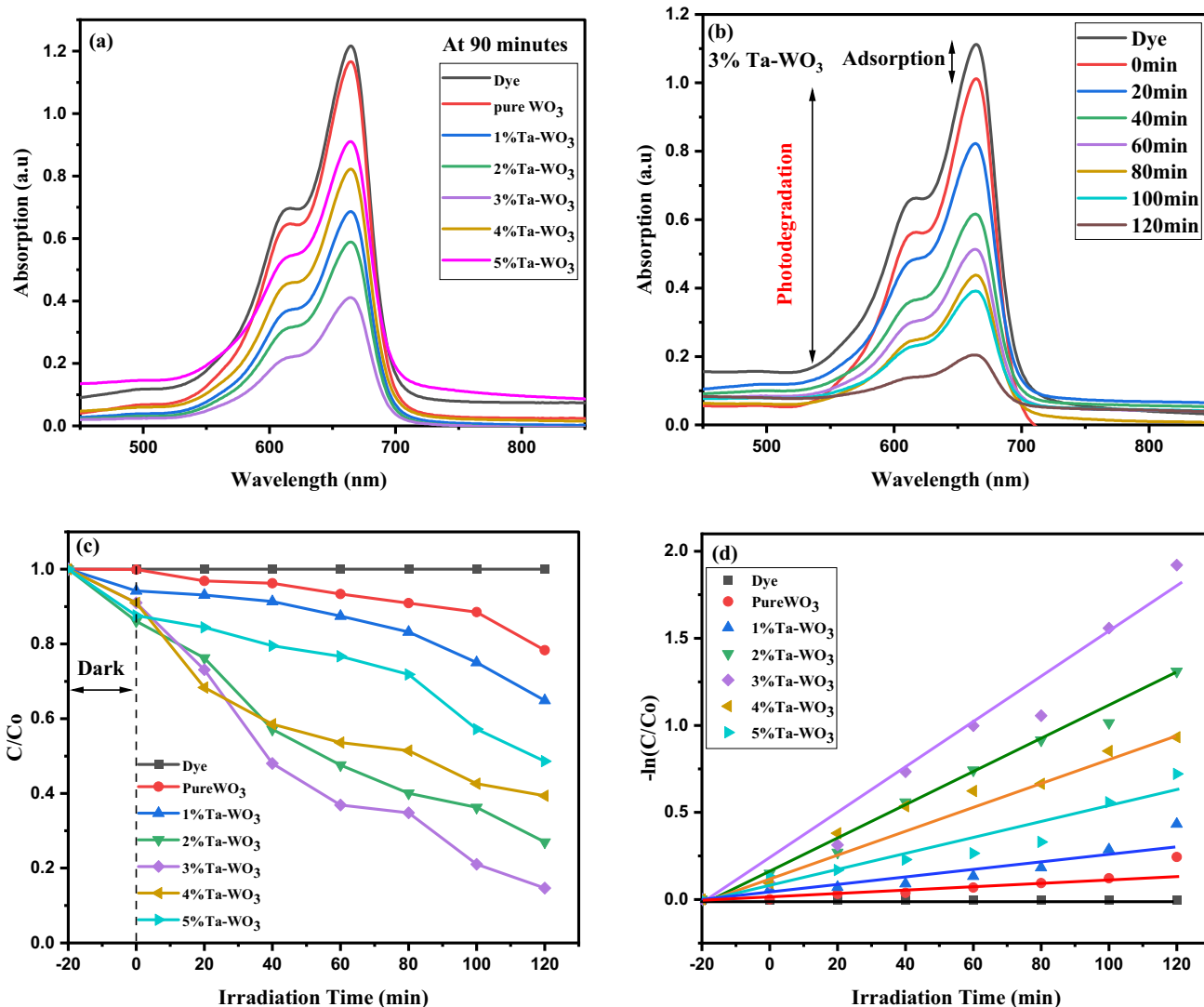


Fig. 8 a UV–Vis spectrum for photocatalytic activity of pure and 1–5% Ta-doped WO₃ at 90 min b UV–Vis double beam spectrum for photocatalytic activity of most optimized concentration 3% Ta-doped

WO₃ till 120 min c Degradation efficiency w.r.t time for pure and Ta-doped WO₃ nanoparticles d First-order kinetics for pure and doped WO₃ nanoparticles

Table 1 Represents the first order kinetic constant “k” and regression analysis for pure and Ta-doped WO₃ nanoparticles

Sr. No	Material	1st Order Kinetic Constant “k” (min ⁻¹)	Correlation coefficient, R ²
1	Pure WO ₃	0.0020348	0.86014
2	1% Ta-doped WO ₃	0.0036082	0.93679
3	2% Ta-doped WO ₃	0.0109128	0.97375
4	3% Ta-doped WO ₃	0.0160013	0.98474
5	4% Ta-doped WO ₃	0.0060081	0.83614
6	5% Ta-doped WO ₃	0.0077641	0.82223

exposed to light with a threshold frequency. As a result, these electrons move towards the conduction band, leading to the production of same number of holes in the valence band, as reported [52, 53]. The WO₃ ions in the system absorb the photo-generated electrons, which create reactive oxygen species (ROS) superoxide anion radical, hydrogen peroxide, singlet oxygen, and hydroxyl ion as shown in Fig. 9. In this manner, WO₃ functions as a quencher/scavenger, reducing the recombination rate of electron and holes. The following are the mathematical formulations:

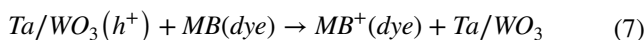
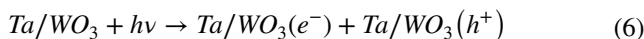
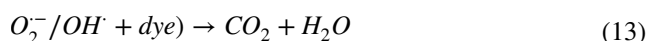
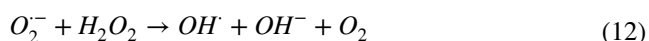
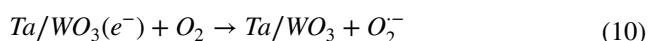
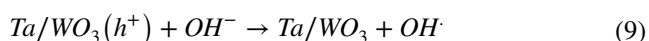
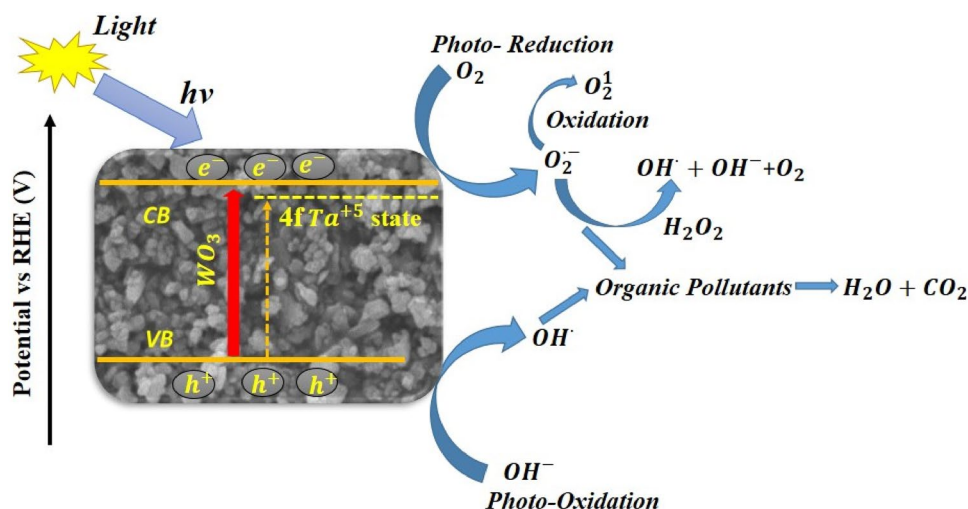


Fig. 9 Schematic representation of the band structure of Ta/WO₃ which is based on the analysis of optical, electrochemical, and valence band edge results



Water causes the formation of OH⁻ and H⁺ ions when the Ta/WO₃ catalyst is used. The positively charged MB dye is produced when the holes combine with it.

It is reported that the reaction between oxygen O₂ and electrons generates the superoxide anion radical. The OH⁻ and radicals combine to create peroxide radicals and hydrogen ions. These peroxide radicals and hydrogen ions react with the superoxide anion and hydroxyl radicals to create strong oxidants that then react with MB, converting them into CO₂ and water [54]. The degradation mechanism for photocatalysis is illustrated in Fig. 9.

3.7.1 Radical Scavenger Analysis

Trapping experiments have been carried out using different scavengers, such as Ascorbic Acid (AA), Methanol, and Isopropanol (IPA), which have been reported to trap superoxide radical •O₂⁻, holes (h⁺), and hydroxyl radical •OH produced in the reaction mixture on excitation of semiconducting material. To understand the photocatalytic mechanism and to examine the impact of the main reactive species

in the photocatalytic degradation mechanism, the variation in MB concentration as a function of irradiation duration is depicted in Fig. 10a both in the absence and presence of different scavengers that include 3% Ta-doped WO₃ photocatalyst. The findings suggest that scavengers like AA and IPA have a significant impact on slowing down the degradation rate, demonstrating that •O₂⁻ and •OH are the primary reactive species in the breakdown of MB. The comparative study of current research work with literature is described in Table 2.

3.7.2 Recyclability of Optimized Photocatalyst

The stability of the photocatalyst was tested for recyclability because it is crucial from an application aspect. The catalyst 3% Ta-doped WO₃ was retrieved by checking its stability from this experiment after being used. In the photochemical experiment, the material was cleaned with acetone and water many times to get rid of the undesired material. It was then dried at 80 °C for 3 h and utilized in the next experiment. The % degradation of the dye, as shown in Fig. 10b, led to only a little reduction in the photocatalytic efficiency of the catalyst after seven subsequent uses of 3% Ta-doped WO₃ for the degradation of MB, demonstrating enhanced photocatalytic stability of the substance.

4 Conclusions

In this current work, pure and Ta-doped WO₃ having various concentrations of 1 to 5% nanoparticles were synthesized for photocatalytic degradation of MB dye. The eco-friendly hydrothermal synthesis method was successfully used. The slight shift in peaks of XRD and Raman, decrease in crystallinity, and reduced band gap represent successful doping of Ta. Introducing 3% Ta⁺⁵ ions into

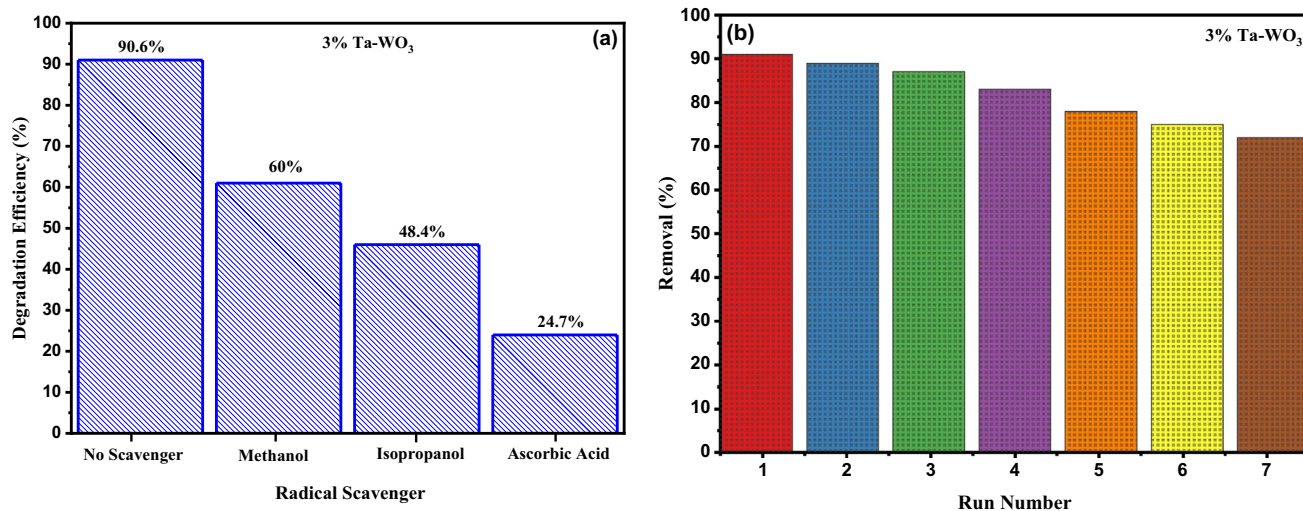


Fig. 10 **a** Effect of different radical scavengers on catalytic efficiency of 3% Ta-doped WO₃. **b** Highlighting the stability of optimized 3% Ta-doped WO₃ catalyst for the degradation of MB after seven cycles

Table 2 Comparison of current research work with previous studies reported in literature

Sr. No	Photocatalyst	Methodology	Model pollutant	Degradation (%)	References
1	S/WO ₃	Hydrothermal	MB	78.7	[55]
2	WO ₃	Hydrothermal	MB	66.39	[56]
3	Cu/WO ₃	Chemical	Tetracycline (TC)	93.7	[57]
4	Zn/ WO ₃	Microwave Radiation	RhB	43	[58]
5	Ta/ WO ₃	Hydrothermal	MB	91	Current research work

WO₃ due to its well-matched ionic radius plays a dynamic role in reducing the recombination rate of photogenerated electrons thus decreasing band gap up to 2.12 and 1.9 eV for direct and indirect transitions respectively. SEM analysis was done to examine the morphology and average size of NPs by histogram. These results were well-correlated to the crystallite size of NPs analyzed by XRD i-e 15.72 and 11.32 nm for pure and 3% Ta/WO₃ respectively. It is worth mentioning that two different phases of WO₃ monoclinic and hexagonal were analyzed by both XRD and Raman analysis. Photocatalytic activity and recyclability were performed for the degradation of MB dye under visible light irradiation for which 3% Ta-doped WO₃ catalyst shows optimized results due to maximum degradation in 120 min that promotes its activity and stability. This could be attributed to the strong absorption of visible light in 3% Ta-doped WO₃. A trapping experiment has been performed by using different scavengers which represents that •O₂⁻ and •OH play a significant role in the degradation of MB. Results have led to the suggestion of a potential photodegradation process involving the interaction

of photosensitized and synergistic impact of Ta into the WO₃ catalyst.

Author Contributions IM: contributed about conceptualization, methodology and original/initial draft. TI: contributed towards conceptualization, formal analysis and Supervision. SA and AMA: contributed validation, editing, and review of final draft.

Funding The authors extend their appreciation to the Deanship of Scientific Research at King Khalid University for funding this work through large group Research Project under grant number RGP2/193/44.

Data Availability All data generated or analyzed during this study are included in this published article.

Declarations

Conflict of interest The authors declare that they have no competing interests.

Ethical Approval Not applicable.

Consent to Participate Not applicable.

Consent to Publish Not applicable.

References

- M. Adeel et al., Synthesis and characterization of Co–ZnO and evaluation of its photocatalytic activity for photodegradation of methyl orange. *ACS Omega* **6**(2), 1426–1435 (2021)
- K.B. Daij, S. Bellebia, Z. Bengharez, Comparative experimental study on the COD removal in aqueous solution of pesticides by the electrocoagulation process using monopolar iron electrodes. *Chem. Int* **3**(4), 420–427 (2017)
- M. Verma et al., Efficient photocatalytic degradation of malachite green dye using facilely synthesized cobalt oxide nanomaterials using citric acid and oleic acid. *J. Phys. Chem. Solids* **155**, 110125 (2021)
- K. Chojnacka et al., Progress in sustainable technologies of leather wastes valorization as solutions for the circular economy. *J. Clean. Prod.* **313**, 127902 (2021)
- M. Laissaoui et al., Adsorption of methylene blue on bituminous schists from Tarfaya-Boujdour. *Chem. Int.* **3**(4), 343–352 (2017)
- S. Jafarnejad, Activated sludge combined with powdered activated carbon (PACT process) for the petroleum industry wastewater treatment: a review. *Chem. Int.* **3**(4), 368 (2017)
- R.D. Cortright, R. Davda, J.A. Dumesic, Hydrogen from catalytic reforming of biomass-derived hydrocarbons in liquid water. *Nature* **418**(6901), 964–967 (2002)
- U. Alam et al., Highly efficient Y and V co-doped ZnO photocatalyst with enhanced dye sensitized visible light photocatalytic activity. *Catal. Today* **284**, 169–178 (2017)
- S.S. Kalanur, L.T. Duy, H. Seo, Recent progress in photoelectrochemical water splitting activity of WO₃ photoanodes. *Top. Catal.* **61**, 1043–1076 (2018)
- L. Tan et al., Synergistic effect of adsorption and photocatalysis of 3D g-C₃N₄-agar hybrid aerogels. *Appl. Surf. Sci.* **467**, 286–292 (2019)
- H.-Y. Liu et al., Facile assembly of g-C₃N₄/Ag₂CO₃/graphene oxide with a novel dual Z-scheme system for enhanced photocatalytic pollutant degradation. *Appl. Surf. Sci.* **475**, 421–434 (2019)
- Q. Li et al., Noble-metal-free amorphous CoMoS_x modified CdS core-shell nanowires for dramatically enhanced photocatalytic hydrogen evolution under visible light irradiation. *Appl. Surf. Sci.* **498**, 143863 (2019)
- X.-Q. Qiao et al., In situ synthesis of n–n Bi₂MoO₆ & Bi₂S₃ heterojunctions for highly efficient photocatalytic removal of Cr(VI). *J. Mater. Chem. A* **6**(45), 22580–22589 (2018)
- M. Rezaeyenik, M. Mousavi-Kamazani, S. Zinatloo-Ajabshir, CeVO₄/rGO nanocomposite: facile hydrothermal synthesis, characterization, and electrochemical hydrogen storage. *Appl. Phys. A* **129**(1), 47 (2023)
- M.S. Morassaei, S. Zinatloo-Ajabshir, M. Salavati-Niasari, Nd₂Sn₂O₇ nanostructures: new facile Pechini preparation, characterization, and investigation of their photocatalytic degradation of methyl orange dye. *Adv. Powder Technol.* **28**(3), 697–705 (2017)
- M.H. Esfahani et al., Structural characterization, phase analysis and electrochemical hydrogen storage studies on new pyrochlore SmRETi₂O₇ (RE = Dy, Ho, and Yb) microstructures. *Ceram. Int.* **49**(1), 253–263 (2023)
- Biswasa, B.D., M.D. Purkayasthab, and T.P. Majumderb, *Surfaces and Interfaces*.
- S. Zinatloo-Ajabshir, E. Shafaati, A. Bahrami, Facile fabrication of efficient Pr₂Ce₂O₇ ceramic nanostructure for enhanced photocatalytic performances under solar light. *Ceram. Int.* **48**(17), 24695–24705 (2022)
- K. Mahdavi et al., Enhanced photocatalytic degradation of toxic contaminants using Dy₂O₃-SiO₂ ceramic nanostructured materials fabricated by a new, simple and rapid sonochemical approach. *Ultrason. Sonochem.* **82**, 105892 (2022)
- S. Zinatloo-Ajabshir et al., Green synthesis, characterization and investigation of the electrochemical hydrogen storage properties of Dy₂Ce₂O₇ nanostructures with fig extract. *Int. J. Hydrogen Energy* **44**(36), 20110–20120 (2019)
- S. Zinatloo-Ajabshir, M. Salavati-Niasari, Zirconia Nanostructures: novel facile surfactant-free preparation and characterization. *Int. J. Appl. Ceram. Technol.* **13**(1), 108–115 (2016)
- S. Mortazavi-Derazkola, S. Zinatloo-Ajabshir, M. Salavati-Niasari, Preparation and characterization of Nd₂O₃ nanostructures via a new facile solvent-less route. *J. Mater. Sci.: Mater. Electron.* **26**, 5658–5667 (2015)
- U. Alam, K. Pandey, N. Verma, Photocatalytic oxidation of glyphosate and reduction of Cr(VI) in water over ACF-supported CoNiWO₄-gCN composite under batch and flow conditions. *Chemosphere* **297**, 134119 (2022)
- U. Alam, N. Verma, Direct Z-scheme-based novel cobalt nickel tungstate/graphitic carbon nitride composite: enhanced photocatalytic degradation of organic pollutants and oxidation of benzyl alcohol. *Coll. and Surf. A: Physicochem. Eng. Aspects* (2021). <https://doi.org/10.1016/j.colsurfa.2021.127606>
- Y. Qu, X. Duan, Progress, challenge and perspective of heterogeneous photocatalysts. *Chem. Soc. Rev.* **42**(7), 2568–2580 (2013)
- C.G. Joseph et al., Application of plasmonic metal nanoparticles in TiO₂-SiO₂ composite as an efficient solar-activated photocatalyst: a review paper. *Front. Chem.* **8**, 568063 (2021)
- V. Etacheri et al., Visible-light activation of TiO₂ photocatalysts: advances in theory and experiments. *J. Photochem. Photobiol. C* **25**, 1–29 (2015)
- P.V.L. Reddy et al., TiO₂-based photocatalytic disinfection of microbes in aqueous media: a review. *Environ. Res.* **154**, 296–303 (2017)
- B. Zhang et al., In situ synthesis of ultrafine TiO₂ nanoparticles modified g-C₃N₄ heterojunction photocatalyst with enhanced photocatalytic activity. *Sep. Purif. Technol.* **247**, 116932 (2020)
- A. Gomis-Berenguer et al., Nanoporous carbon/WO₃ anodes for an enhanced water photooxidation. *Carbon* **108**, 471–479 (2016)
- M. Gondal et al., Preparation of WO₃/gC₃N₄ composites and their enhanced photodegradation of contaminants in aqueous solution under visible light irradiation. *React. Kinet. Mech. Catal.* **114**, 357–367 (2015)
- C. Yu et al., Grinding calcination preparation of WO₃/BiOCl heterostructures with enhanced visible light photocatalytic activity. *Mater. Res. Innov.* **19**(1), 54–59 (2015)
- W. Zhang et al., Photocatalytic degradation of azophloxine on porous La₂Ti₂O₇ prepared by sol-gel method. *Solid State Sci.* **87**, 58–63 (2019)
- W. Zhang, J. Yang, C. Li, Role of thermal treatment on sol-gel preparation of porous cerium titanate: characterization and photocatalytic degradation of ofloxacin. *Mater. Sci. Semicond. Process.* **85**, 33–39 (2018)
- J.Y. Luo et al., Strong aggregation adsorption of methylene blue from water using amorphous WO₃ nanosheets. *Appl. Surf. Sci.* **287**, 270–275 (2013)
- S. Jeon, K. Yong, Morphology-controlled synthesis of highly adsorptive tungsten oxide nanostructures and their application to water treatment. *J. Mater. Chem.* **20**(45), 10146–10151 (2010)
- H. Ou, D. Wang, Y. Li, How to select effective electrocatalysts: Nano or single atom? *Nano Select* **2**(3), 492–511 (2021)
- Y. Pan et al., Active sites in heterogeneous catalytic reaction on metal and metal oxide: theory and practice. *Catalysts* **8**(10), 478 (2018)
- H. Lin et al., Prussian blue/PVDF catalytic membrane with exceptional and stable Fenton oxidation performance for organic pollutants removal. *Appl. Catal. B* **273**, 119047 (2020)

40. B. Song et al., Two-step hydrothermally synthesized carbon nano-dots/WO₃ photocatalysts with enhanced photocatalytic performance. *Dalton Trans.* **46**(45), 15769–15777 (2017)
41. S.S. Kalanur, H. Seo, Aligned nanotriangles of tantalum doped tungsten oxide for improved photoelectrochemical water splitting. *J. Alloy. Compd.* **785**, 1097–1105 (2019)
42. S.S. Kalanur, I.-H. Yoo, H. Seo, Fundamental investigation of Ti doped WO₃ photoanode and their influence on photoelectrochemical water splitting activity. *Electrochim. Acta* **254**, 348–357 (2017)
43. P. Kaur et al., Influence of defect structure on colour tunability and magneto optical behaviour of WO₃ nanoforms. *RSC Adv.* **9**(36), 20536–20548 (2019)
44. R. Bhargava, S. Khan, Fabrication of WO₃-reduced graphene oxide (WO₃-G) nanocomposite for enhanced optical and electrical properties. *J. Mater. Sci.: Mater. Electron.* **31**, 8370–8384 (2020)
45. W. Song et al., Exposed crystal facets of WO₃ nanosheets by phase control on NO₂-sensing performance. *J. Mater. Sci.: Mater. Electron.* **31**, 610–620 (2020)
46. Z. Wang, S. Zhou, L. Wu, Preparation of rectangular WO₃-H₂O nanotubes under mild conditions. *Adv. Func. Mater.* **17**(11), 1790–1794 (2007)
47. I. Aslam et al., Synthesis of WO₃-H₂O spherical particles for efficient photocatalytic properties under visible light source. *Mater. Sci. Energy Technol.* **2**(2), 187–193 (2019)
48. M. Dinari, M.M. Momeni, M. Ahangarpour, Efficient degradation of methylene blue dye over tungsten trioxide/multi-walled carbon nanotube system as a novel photocatalyst. *Appl. Phys. A* **122**, 1–9 (2016)
49. P. Gairola et al., Enhanced electromagnetic absorption in ferrite and tantalum pentoxide based polypyrrole nanocomposite. *Prog. Nat. Sci.: Mater. Int.* **29**(2), 170–176 (2019)
50. F.S. Tehrani, H. Ahmadian, M. Aliannezhadi, Hydrothermal synthesis and characterization of WO₃ nanostructures: effect of reaction time. *Mater. Res. Exp.* **7**(1), 015911 (2020)
51. W.A. El-Yazeed, A.I. Ahmed, Photocatalytic activity of mesoporous WO₃/TiO₂ nanocomposites for the photodegradation of methylene blue. *Inorg. Chem. Commun.* **105**, 102–111 (2019)
52. A. Fujii et al., Preparation of Pt-loaded WO₃ with different types of morphology and photocatalytic degradation of methylene blue. *Surf. Coat. Technol.* **271**, 251–258 (2015)
53. X. Yin, L. Liu, F. Ai, Enhanced photocatalytic degradation of methylene blue by WO₃ nanoparticles under nir light irradiation. *Front. Chem.* **9**, 683765 (2021)
54. Z. He et al., Photocatalytic degradation of rhodamine B by Bi₂WO₆ with electron accepting agent under microwave irradiation: mechanism and pathway. *J. Hazard. Mater.* **162**(2–3), 1477–1486 (2009)
55. G. Chen et al., Synthesis and photocatalytic activity study of S-doped WO₃ under visible light irradiation. *Environ. Sci. Pollut. Res.* **27**, 15103–15112 (2020)
56. J. Li et al., Synthesis of vertical WO₃ nanoarrays with different morphologies using the same protocol for enhanced photocatalytic and photoelectrocatalytic performances. *RSC Adv.* **11**(38), 23700–23706 (2021)
57. V.T. Quyen et al., Enhanced the visible light photocatalytic decomposition of antibiotic pollutant in wastewater by using Cu doped WO₃. *J. Environ. Chem. Eng.* **9**(1), 104737 (2021)
58. X. Ding et al., Application of WO₃ and Zn-doped WO₃ prepared by microwave irradiation for photocatalytic degradation of Rhodamine B in water and wastewater. *Int. J. Electrochem. Sci* **17**(221045), 2 (2022)

Publisher's Note Springer Nature remains neutral with regard to jurisdictional claims in published maps and institutional affiliations.

Springer Nature or its licensor (e.g. a society or other partner) holds exclusive rights to this article under a publishing agreement with the author(s) or other rightsholder(s); author self-archiving of the accepted manuscript version of this article is solely governed by the terms of such publishing agreement and applicable law.